Supporting Information

Fe-doping Induced Divergent Growth of Ni-Fe Alloy Nanoparticles for

Enhancing Electrocatalytic Oxygen Reduction

Qianjie Xie,[a#] Zheng Wang,[*b#] Chen Lei,[c] Penghu Guo,[d] Cong Li,[a] Yehua Shen,[*a] Hiroshi Uyama[a, e]

[a.]Key Laboratory of Synthetic and Natural Functional Molecule Chemistry of Ministry of Education, College of Chemistry and Materials Science, Northwest University, 710127 Xi'an, Shaanxi, China.
[b.]College of Food Science and Engineering, Northwest University, 710069 Xi'an, Shaanxi, China.
[c.]Department of Physical and Macromolecular Chemistry, Faculty of Science, Charles University, Hlavova 8, 128 43 Praha 2, Czech Republic.
[d.]School of Chemistry, Guangdong University of Petrochemical Technology, 525000 Maoming, Guangdong, China.
[#]These authors contributed equally to this work.
Corresponding author: Dr. Zheng Wang; email: zheng.wang@nwu.edu.cn

Experimental

OER tests. 11 µL of the catalyst ink was loaded on a glassy carbon electrode (GCE) with 3 mm diameter (loading amount: ~0.30 mg cm^{-2}) for oxygen evolution reaction (OER) tests. The commercial IrO_2 electrode was employed as reference. All of the tests were performed with a graphite electrode counter electrode. Cyclic voltammetry (CV) measurements were carried out in 1 M KOH solution for with a scan rate of 50 mV s^{-1}. Linear sweep voltammetry (LSV) curves were recorded under the same electrolyte with a scan rate of 5 mV s^{-1}. All the measured OER polarization curve potentials in this work were performed with iR compensation. The stability tests for OER were conducted by coating electrocatalyst ink on the side of carbon cloth (1.5 × 1 cm) with a loading amount of 0.30 mg cm^{-2}. The electrochemical impedance spectroscopy (EIS) measurements were recorded in a frequency range from 100 kHz to 1 Hz with amplitude of 5 mV at an applied potential of 1.6 V vs. RHE. The electrochemically active surface area (ECSA) was measured by the electrochemical double-layer capacitance (C_{dl}) in a non-Faradaic potential range of 1.024–1.124 V vs RHE at different scan rates of 4, 8, 12, 16 and 20 mV s^{-1}.

Discussion

X-ray diffraction. The powder X-ray diffraction (XRD) pattern of $Ni_{0.8}Fe_{0.2}BDP/GO$ precursor matches well with the simulated MOF, and the additional peaks at 11° can be indexed into GO, which confirms the successful synthesis of hybrid $Ni_{0.8}Fe_{0.2}BDP$ MOF and GO (Figure S1a). The XRD patterns of derived $Ni_{1-x}Fe_x@NC/rGO$ (x = 0, 0.05, 0.1, 0.2 and 0.3) are shown in Figure 3a in paper. The diffraction peaks around at 44.3°, 51.5° and 75.9° of $Ni_{0.8}Fe_{0.2}BDP/GO$ characteristic for the (111), (200) and (220) reflections of NiFe alloy and Ni. A broad shoulder peak between 20° and 30° originates from the (002) plane of graphitic carbon.[1]

Fourier transformation infrared spectroscopy. The broad peaks at 3300 cm^{-1}, 1580 cm^{-1}, 1630 cm^{-1} in Fourier transformation infrared (FT-IR) spectrum of MOF $Ni_{0.8}Fe_{0.2}BDP/GO$ associate with the functional groups of GO and the rest peaks are corresponding to NiFeBDP.[2] FT-IR verified the successful synthesis of hybrid $Ni_{0.8}Fe_{0.2}BDP$ MOF and GO, which is corresponding to the XRD results (Figure S1b).

Element confirmation. The N contents of $Ni_{1-x}Fe_x@NC/rGO$ (x = 0, 0.05, 0.1, 0.2 and 0.3) were measured to be about 5 w.t.% by elemental analysis (EA). High N content substitution could strengthen the OH desorption as well as hydrogenation that accounts for the enhanced ORR performance.[3] The molar ratios of Ni/Fe in the electrocatalysts of $Ni_{0.95}Fe_{0.05}@NC/rGO$, $Ni_{0.9}Fe_{0.1}@NC/rGO$, $Ni_{0.8}Fe_{0.2}@NC/rGO$ and $Ni_{0.7}Fe_{0.3}@NC/rGO$ were calculated to be 5.36 w.t.%, 11.65 w.t.%, 19.21 w.t.% and 42.27 w.t.% by inductively coupled plasma mass spectrometry (ICP-MS) and energy-dispersive X-ray spectroscopy (EDS) kx-Spectra (Figure S3), respectively. All of the ratios were reasonable regulated. Due to Fe owning more superiority than Ni in competition

coordination, the content of Fe exceeds feed ratio in the sample of $Ni_{0.7}Fe_{0.3}$@NC/rGO.

Raman spectra. More information about carbon species in catalysts derived under different temperature is provided by Raman spectra (Figure S6). All samples displayed two clearly separated peaks: the D band at 1330 cm^{-1} corresponded to the structural defects in graphitic structure, while the G band at 1590 cm^{-1} arose from sp^2-bonded pairs. The intensity ratios (I_D/I_G) were calculated to be 1.12, 1.12, 1.18 for 700 °C-1h, 800 °C-1h, 900 °C-1h, respectively, indicating the low graphitization degree and high defect density of obtained electrocatalysts.

OER activity of electrocatalysts. The OER activity of $Ni_{1-x}Fe_x$@NC/rGO (x = 0, 0.05, 0.1, 0.2 and 0.3) were investigated in a standard three-electrode cell with 1.0 M KOH aqueous solution by employing IrO_2 as reference. Viewing from the LSV curves, shown in Figure S11a, $Ni_{0.8}Fe_{0.2}$@NC/rGO exhibits better activity than other catalyst. The overpotential correlated at j = 10 mA cm^{-2} was 407 mV for $Ni_{0.8}Fe_{0.2}$@NC/rGO, which is slightly higher than that of the reference IrO_2 (360 mV). Tafel analysis (Figure. S11b) indicates that the Tafel slope of $Ni_{0.8}Fe_{0.2}$@NC/rGO (66.77 mV/dec) is smaller than other control cases and also very close to the IrO_2 (62.57 mV/dec), demonstrating its favorable OER reaction rate.[4] Moreover, charge transfer resistance (RCT), electrochemically active surface area (ECSA), and durability of $Ni_{1-x}Fe_x$@NC/rGO were further evaluated and related data are shown in Figure S11c–d and S12. The analysis of these data manifests that the catalyst with 20% Fe doping shows the better OER activity and durability than other cases and many reported cases.[5]
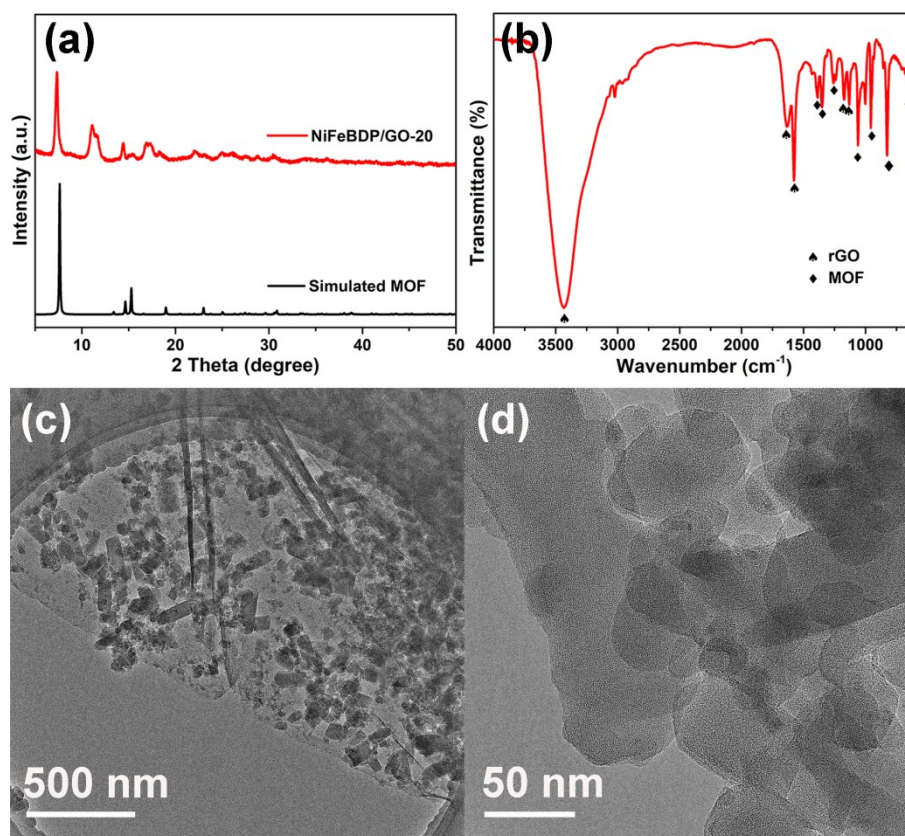
Figure S1. (a) XRD, (b) FT-IR spectroscopy and (c) transmission electron microscope (TEM) of Ni$_{0.8}$Fe$_{0.2}$BDP/GO precursor.
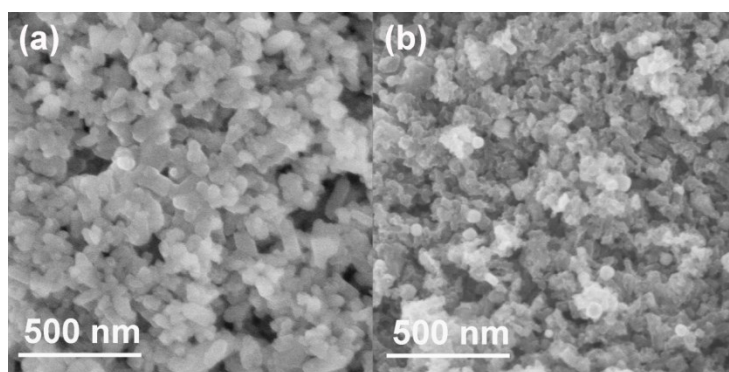
Figure S2. Scanning electron microscopy (SEM) images of (a) $Ni_{0.8}Fe_{0.2}BDP/GO$ and (b) derived $Ni_{0.8}Fe_{0.2}@NC/rGO$.
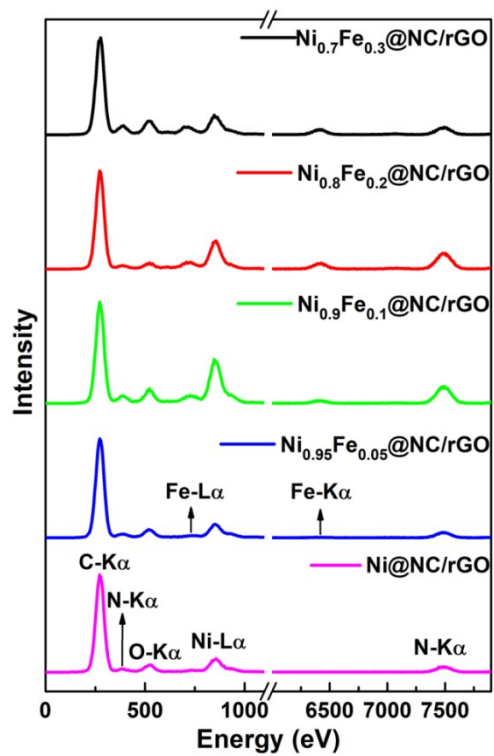
Figure S3. Energy dispersive X-ray (EDX) spectra of the electrocatalyst of $Ni_{1-x}Fe_x$@NC/rGO (x = 0, 0.05, 0.1, 0.2 and 0.3).
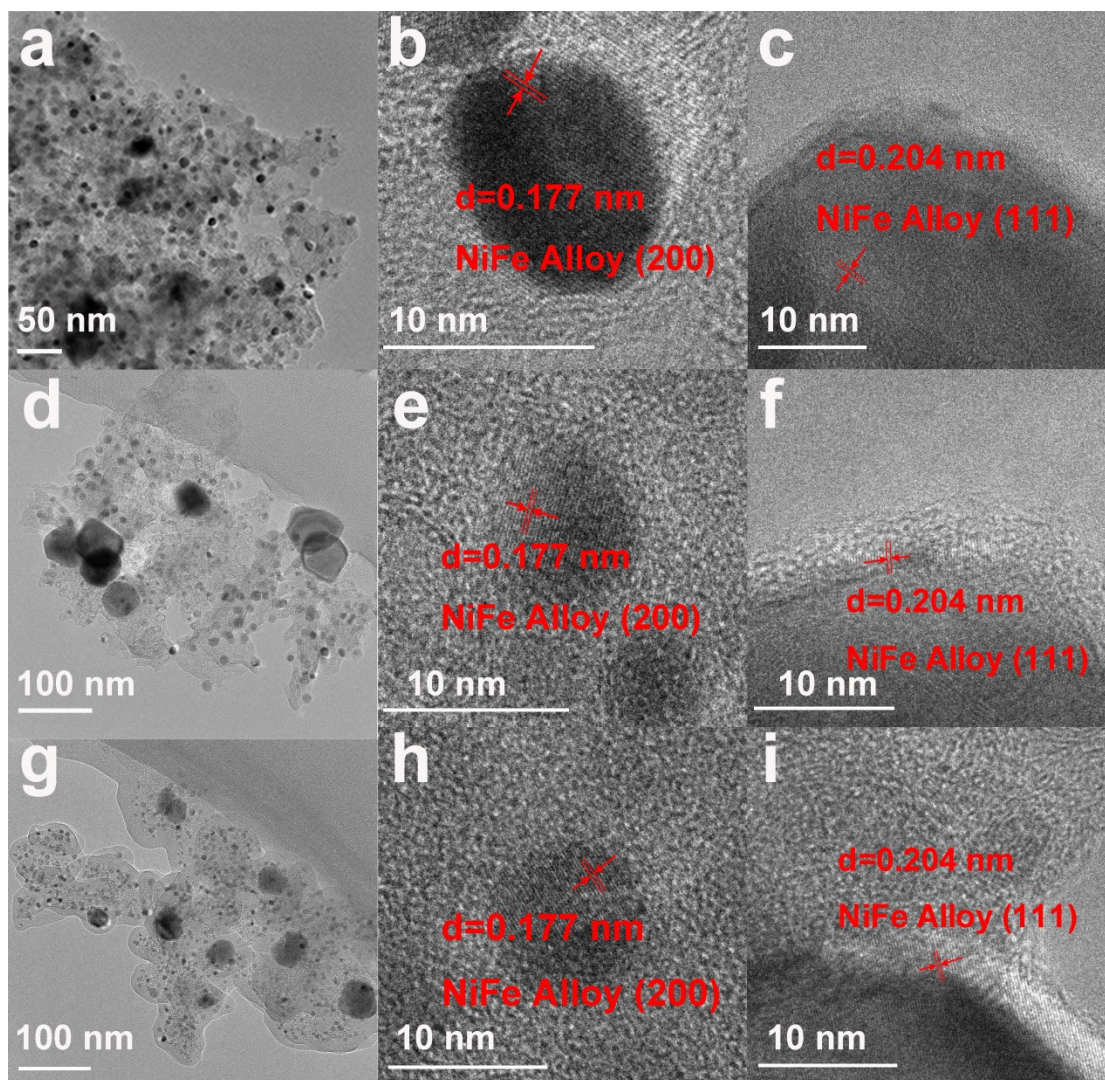
Figure S4. TEM images of catalysts and lattice fringes of nanoparticles: (a-c) Ni@NC/rGO, Ni$_{0.95}$Fe$_{0.05}$@NC/rGO, (d–f) Ni$_{0.9}$Fe$_{0.1}$@NC/rGO and (g–i) Ni$_{0.7}$Fe$_{0.3}$@NC/rGO.
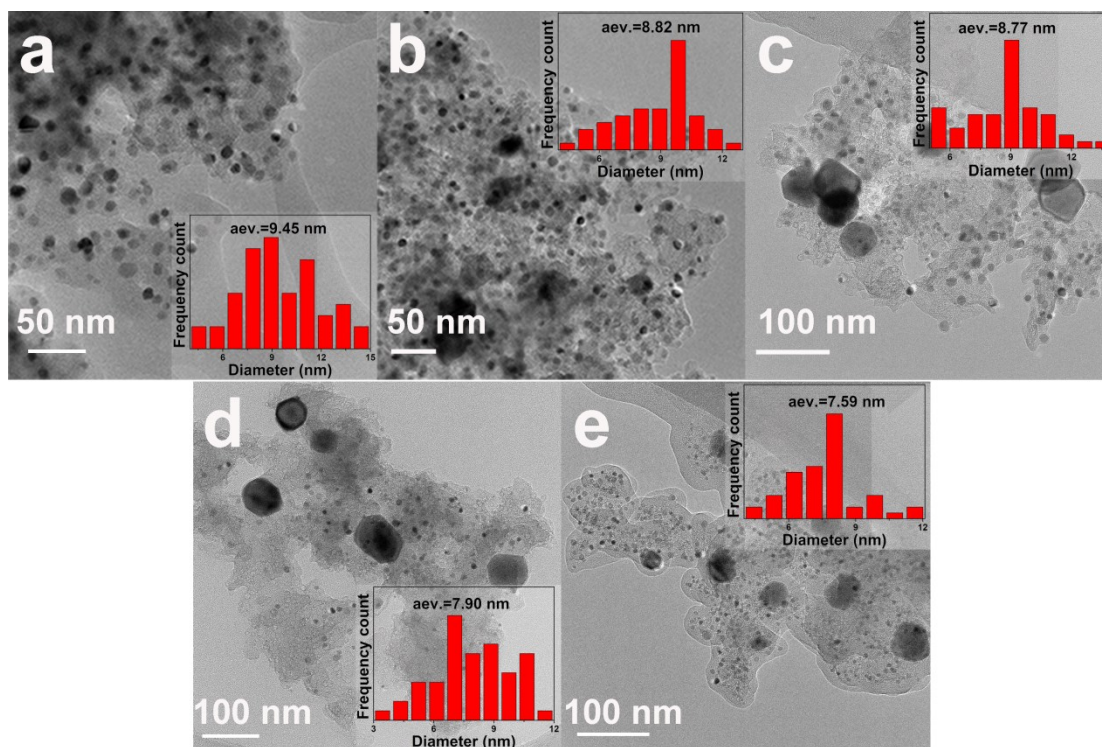
Figure S5. The size distribution of $Ni_{1-x}Fe_x(200)$ NPs within $Ni_{1-x}Fe_x@NC/rGO$ (x = 0-a, 0.05-b, 0.1-c, 0.2-d and 0.3-e). Herein, the size of (111)-faceted NPs increases with raising the doping amount of Fe (32 nm for $Ni_{0.95}Fe_{0.05}$, 52 nm for $Ni_{0.9}Fe_{0.1}$, 55 nm for $Ni_{0.8}Fe_{0.2}$ and 58 nm for $Ni_{0.7}Fe_{0.3}$). The relative number ratios of (111)- and (200)-faceted NPs are 1 : 37, 1 : 20, 1 : 26 and 1 : 24 for $Ni_{1-x}Fe_x@NC/rGO$ (x = 0, 0.05, 0.1, 0.2 and 0.3), respectively.
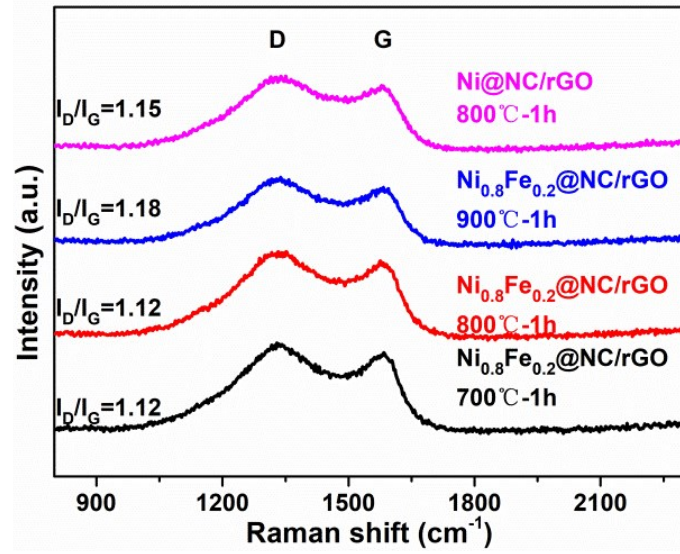
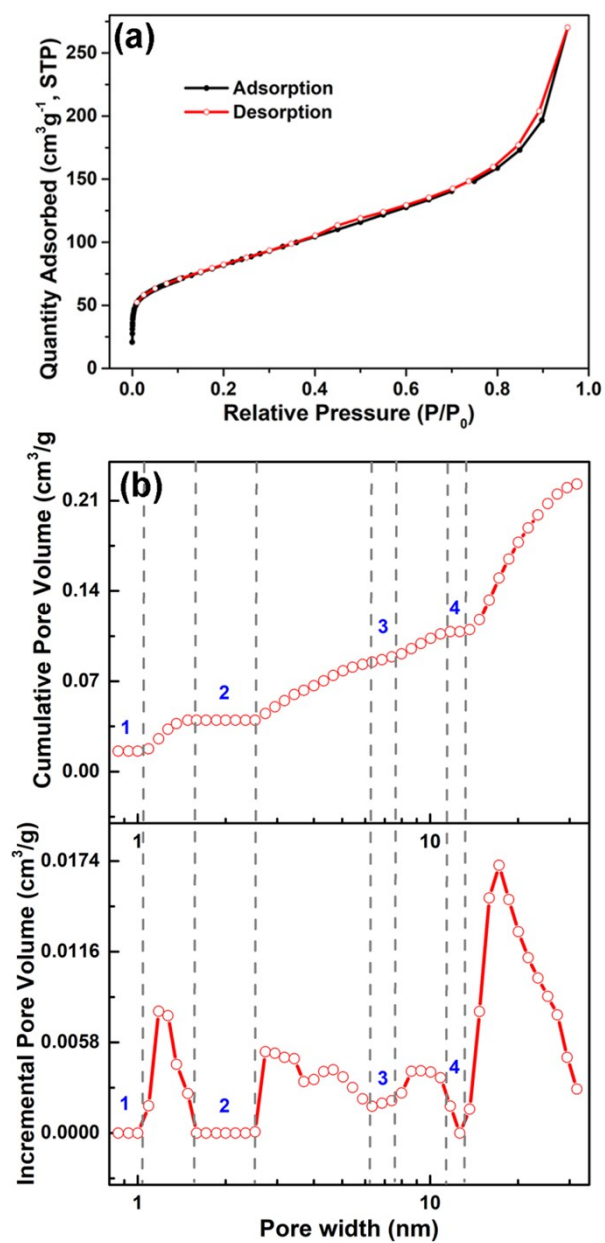**Figure S6.** Raman spectra of $Ni_{0.8}Fe_{0.2}$@NC/rGO catalysts prepared under different temperature.

Figure S7. (a) The N_2 sorption isotherm, and (b) incremental pore volume vs. pore width and (c) cumulative pore volume vs. pore width plots of $Ni_{0.8}Fe_{0.2}@NC/rGO$.

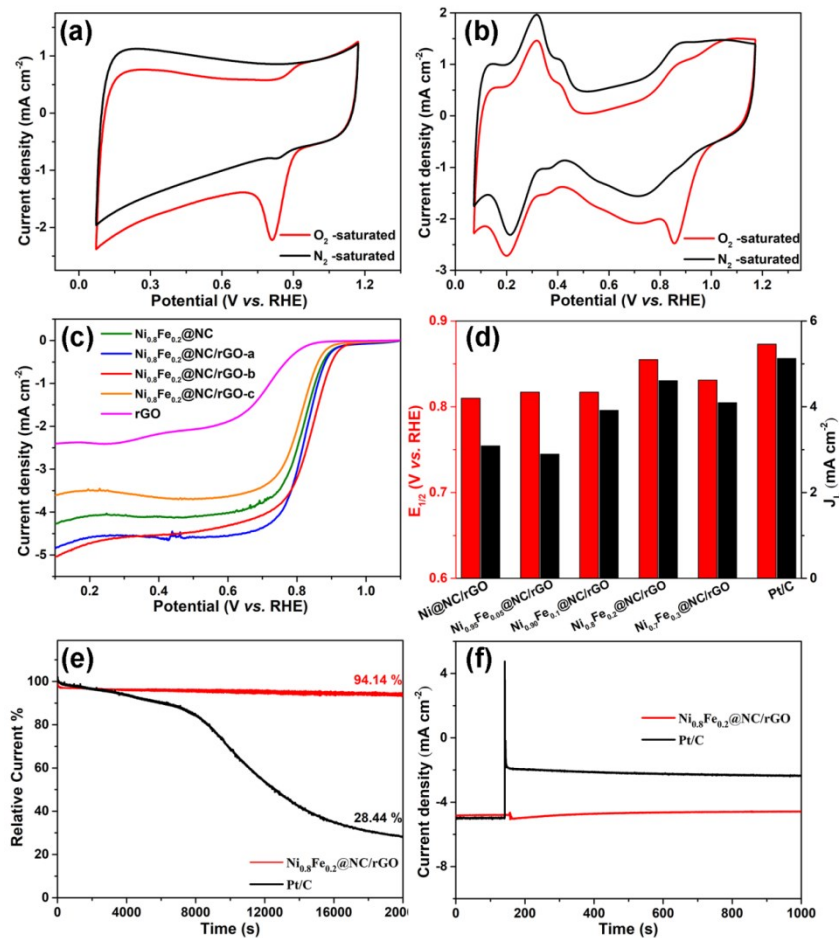**Figure S8.** CV curves of (a) $Ni_{0.8}Fe_{0.2}@NC/rGO$ and (b) 20% Pt/C in O_2- (red)and N_2-saturated (black) 0.1 M KOH at 50 mV s^{-1}; (c) LSV curves of electrocatalysts prepared with different GO content (a, b and c is 6 mg, 12 mg and 24 mg, respectively); (d) summarized half-waved potential ($E_{1/2}$) and diffusion-limited current density (J_L) $Ni_{1-x}Fe_x@NC/rGO$ (x = 0, 0.05, 0.1, 0.2 and 0.3); (e) amperometric i-t curve of the $Ni_{0.8}Fe_{0.2}@NC/rGO$ and 20% Pt/C at applied potential of 0.5 V; (f) i–t responses for $Ni_{0.8}Fe_{0.2}@NC/rGO$ and 20 % Pt/C at 0.5 V and 1600 rpm with 1.0 M methanol addition at around 150 s.

As shown herein, the amount of added GO also has a significant influence on the ORR activity of derived catalysts. The $E_{1/2}$ enhances from 0.839 V with 6 mg GO, peaks at 0.855 V with 12 mg, and then decreases to 0.819 V with 24 mg. Viewing from the observation, we can find that the addition of GO could efficiently promote the ORR activity of derived catalyst due to its enhancements of conductivity and NPs distribution, but the over addition of GO reduced the activity due to its poor activity ($E_{1/2}$ = 0.710 V).
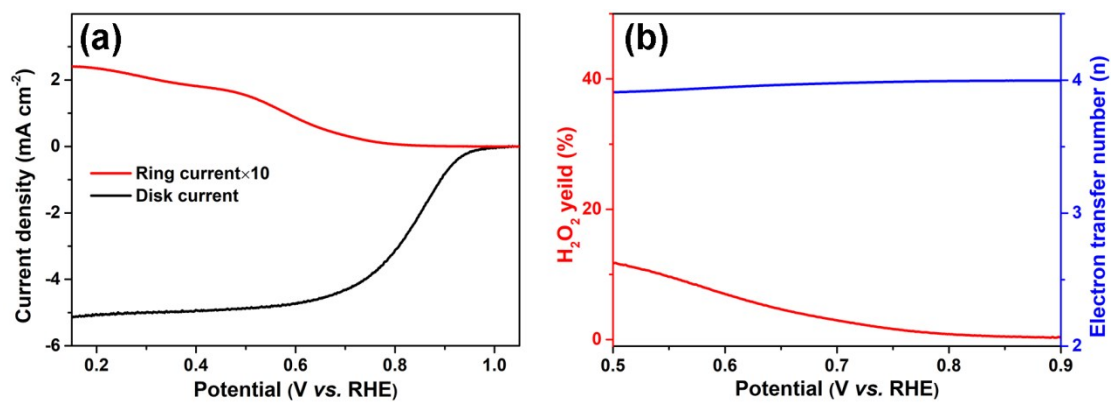
Figure S9. (a) The ORR polarization curve and the corresponding ring current, and (b) the average electron transfer number (n) and H_2O_2 yield of $Ni_{0.8}Fe_{0.2}$@NC/rGO.
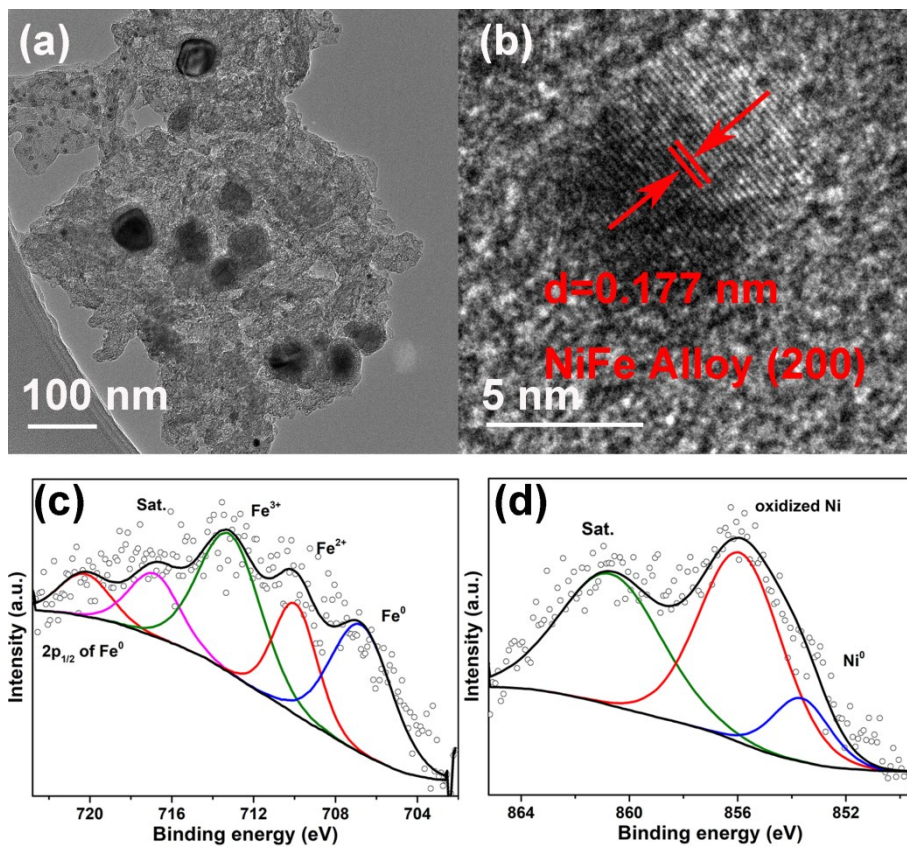
Figure S10. (a) TEM images and (b) lattice fringes of (200)-facetd Ni-Fe alloy NPs of $Ni_{0.8}Fe_{0.2}$@NC/rGO after ORR stability test; (c) Fe 2p and (d) Ni 2P high-resolution XPS spectra of $Ni_{0.8}Fe_{0.2}$@NC/rGO.
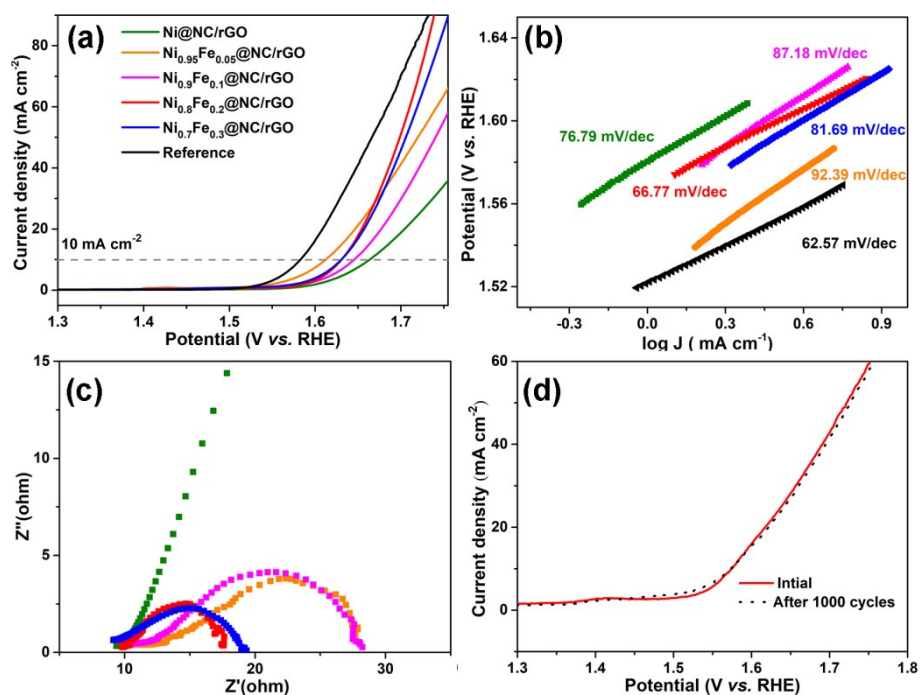
Figure S11. (a) OER polarization of catalysts and reference of IrO_2 catalyst in 1 M of KOH solution at 5 mV s^{-1}, (b) Tafel plots of OER, (c) electrochemical impedance spectroscopy (EIS) Nyquist plots recorded at 1.6 V vs RHE in OER of $Ni_{1-x}Fe_x@NC/rGO$ (x = 0, 0.05, 0.1, 0.2 and 0.3), (d) OER LSV curves recorded for $Ni_{0.8}Fe_{0.2}@NC/rGO$ before and after 1000 cycles, Inset: chronopotentiometry curves at a constant current density of 10 mA cm^{-2}.
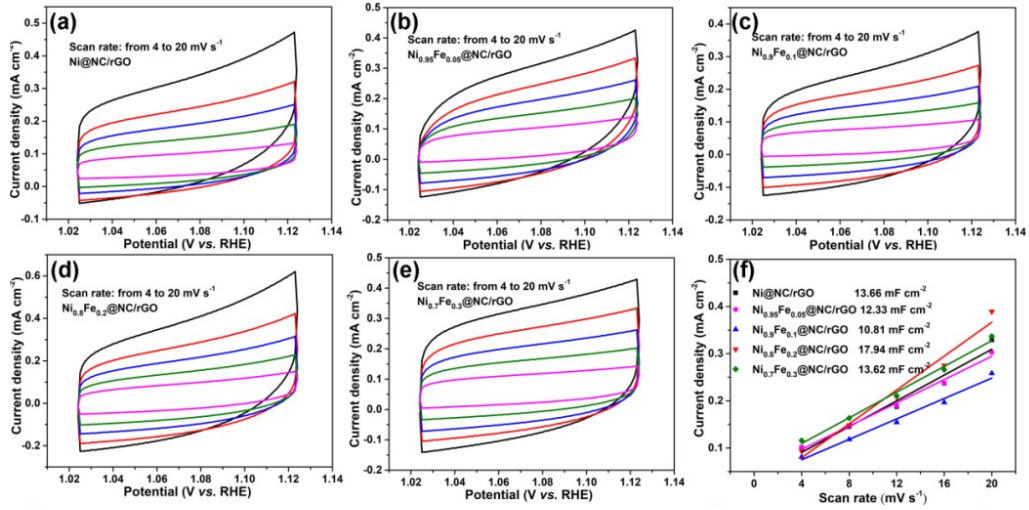
Figure S12. CV curves at different scan rates for (a) Ni@NC/rGO, (b) Ni$_{0.95}$Fe$_{0.05}$@NC/rGO, (c) Ni$_{0.9}$Fe$_{0.1}$@NC/rGO, (d) Ni$_{0.8}$Fe$_{0.2}$@NC/rGO and (e) Ni$_{0.7}$Fe$_{0.3}$@NC/rGO; (f) capacitive i = i*a − i*c at the potential of 1.074 V vs. RHE plotted against scan rate fitted to estimate the electrochemical double-layer capacitances (C$_{dl}$).
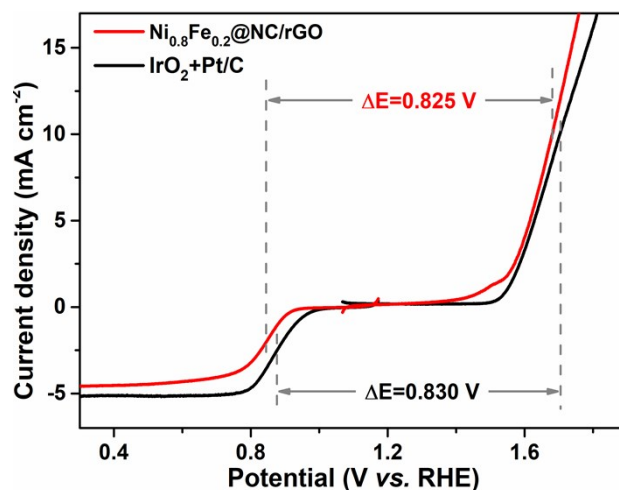
Figure S13. Polarization curves of $Ni_{0.8}Fe_{0.2}$@NC/rGO and 20% Pt/C+IrO_2 in the overall potential range of the ORR and OER ($\Delta E = E_{1/2} - E_{j=10}$). Herein, the OER activities of $Ni_{0.8}Fe_{0.2}$@NC/rGO and IrO_2 were tested in 0.1 M KOH electrolyte at 1600 rpm to evaluate the ΔE. The accurate ΔE of $Ni_{0.8}Fe_{0.2}$@NC/rGO and 20% Pt/C+IrO_2 were 0.825 V (1.68 V - 0.855 V) and 0.830 V (1.703 V - 0.873 V), respectively.
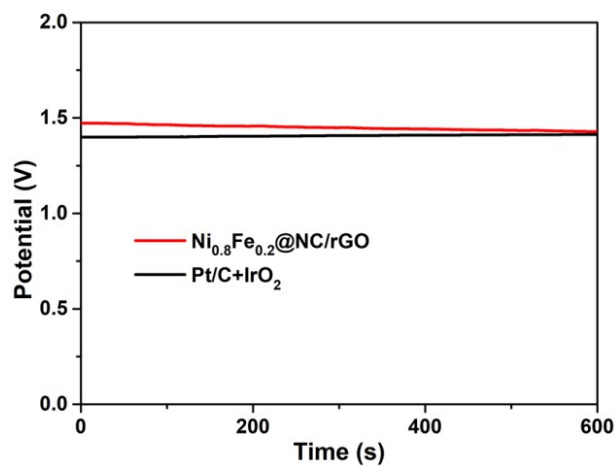
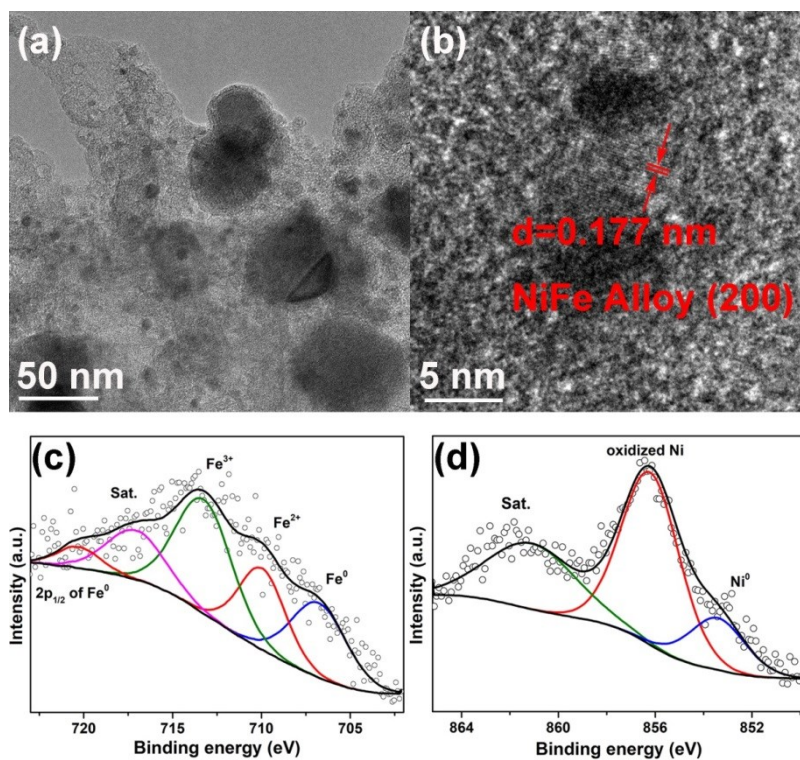**Figure S14.** Open circuit voltages (OCV) of $Ni_{0.8}Fe_{0.2}$@NC/rGO and 20% Pt/C+IrO$_2$ based battery Zn–air batteries.

Figure S15. (a) TEM images and (b) lattice fringes of (200)-faceted Ni-Fe alloy NPs of Ni$_{0.8}$Fe$_{0.2}$@NC/rGO after ZABs stability test; and (c) Fe 2p and (d) Ni 2p high-resolution XPS spectra of Ni$_{0.8}$Fe$_{0.2}$@NC/rGO.

Table S1. The XPS peak position of Ni 2p for Ni(0) and Fe 2p for Fe(0) in $Ni_{1-x}Fe_x$@NC/rGO (x = 0, 0.05, 0.1, 0.2 and 0.3) samples.

Sample name	Ni@NC/rGO	$Ni_{0.95}Fe_{0.05}$@NC/rGO	$Ni_{0.9}Fe_{0.1}$@NC/rGO	$Ni_{0.8}Fe_{0.2}$@NC/rGO	$Ni_{0.7}Fe_{0.3}$@NC/rGO
Binding energy of Ni(0)(eV)	853.17	853.11	853.11	853.07	852.99
Binding energy of Fe(0)(eV)	/	706.74	707.25	707.30	707.41

Table S2. Thermodynamic data used in the binding energy of ORR processes calculations.

Species	Binding energy(eV)	ZPE (eV)	TS (eV)	E_{sol} (eV)
H_2O	/	0.56	0.67	/
H_2	/	0.27	0.41	/
HOO^*- $Ni_{0.8}Fe_{0.2}(111)$	3.42	0.43	0.00	-0.47
O^*- $Ni_{0.8}Fe_{0.2}(111)$	1.31	0.08	0.00	-0.03
HO^*- $Ni_{0.8}Fe_{0.2}(111)$	0.53	0.36	0.00	-0.54
HOO^*- $Ni_{0.8}Fe_{0.2}(200)$	3.50	0.41	0.00	-0.47
O^*- $Ni_{0.8}Fe_{0.2}(200)$	1.42	0.07	0.00	-0.03
HO^*- $Ni_{0.8}Fe_{0.2}(200)$	0.63	0.36	0.00	-0.54
HOO^*- Pt(111)	3.60	0.49	0.00	-0.47
O^*- Pt(111)	1.56	0.09	0.00	-0.03
HO^*- Pt(111)	0.98	0.37	0.00	-0.54

Reference

1.	Z. Lin, H. Huang, L. Cheng, Y. Yang, R. Zhang and Q. Chen, *ACS Sustainable Chem. Eng.*, 2019, **8**, 427.

2.	Z. Wang, Q. Xie, Y. Wang, Y. Shu, C. Li and Y. Shen, *New J. Chem.*, 2020, **44**, 18319.

3.	Q. Wang, L. Shang, R. Shi, X. Zhang, G. I. N. Waterhouse, L.-Z. Wu, C.-H. Tung and T. Zhang, *Nano Energy*, 2017, **40**, 382.

4.	C. Wang, H. Yang, Y. Zhang and Q. Wang, *Angew. Chem. Int. Ed.*, 2019, **58**, 6099.

5.	N. T. Suen, S. F. Hung, Q. Quan, N. Zhang, Y. J. Xu and H. M. Chen, *Chem. Soc. Rev.*, 2017, **46**, 337.